Eco-Environment & Health 3 (2024) 247–255

Contents lists available at ScienceDirect

Eco-Environment & Health

journal homepage: www.journals.elsevier.com/eco-environment-and-health

Original Research Article

Magnetic fields promote electrocatalytic CO_2 reduction via subtle modulations of magnetic moments and molecular bonding

Shilin Wei, Weiqi Liu, Peiyao Bai, Chuangchuang Yang, Xiao Kong, Lang Xu *

MOE Key Laboratory of Coal Processing and Efficient Utilization, School of Chemical Engineering and Technology, China University of Mining and Technology, Xuzhou 221116, China

ARTICLE INFO

Keywords:
External field
Magnetic dependence
Molecular level
Multiphysics coupling

ABSTRACT

Introducing a magnetic-field gradient into an electrically driven chemical reaction is expected to give rise to intriguing research possibilities. In this work, we elaborate on the modes and mechanisms of electrocatalytic activity (from the perspective of alignment of magnetic moments) and selectivity (at the molecular level) for the CO_2 reduction reaction in response to external magnetic fields. We establish a positive correlation between magnetic field strengths and apparent current densities. This correlation can be rationalized by the formation of longer-range ordering of magnetic moments and the resulting decrease in the scattering of conduction electrons and charge-transfer resistances as the field strength increases. Furthermore, aided by the magnetic-field-equipped *operando* infrared spectroscopy, we find that applied magnetic fields are capable of weakening the C–O bond strength of the key intermediate *COOH and elongating the C–O bond length, thereby increasing the faradaic efficiency for the electroreduction of CO_2 to CO.

1. Introduction

The coupling of electric and magnetic fields to catalytic reactions is expected to offer intriguing new possibilities, as Maxwell's equations inform us that these two varying fields can induce each other [1,2]. From this perspective, the application of magnetic fields can have unexpected outcomes for electrochemical processes [3–5]. Due to the paramagnetic property of O_2 and its widespread use in energy and environmental technologies, electrocatalytic O_2 redox reactions in response to external magnetic fields, particularly for O_2 evolution reaction (OER), are under intense investigation [6–8]. Garcés-Pineda et al. observed increases in current density for the OER occurring on highly magnetic Fe–Ni oxides when a magnetic field was applied. They attributed this magnetic enhancement to the spin alignment of oxygen atoms induced by the external field [9]. Subsequently, Xu's group explained how applied magnetic fields increased electrocatalytic activities toward the OER from two aspects: first, spin-polarized electron exchange between a ferromagnetic catalyst $CoFe_2O_4$ and adsorbed O species was found to be facilitated after the application of a magnetic field to $CoFe_2O_4$ [10]; second, magnetization gave rise to the disappearance of domain walls and therefore to the OER activity enhancement [11].

CO_2 is another intriguing molecule that is central to a significant part of the carbon cycle and sustainable development [12–21]. Unlike O_2, CO_2 is diamagnetic, so conclusions drawn from electrocatalytic reactions involving O_2 coupled with external magnetic fields cannot be applied to their CO_2 counterparts, which deserve further investigation. To date, there have been very few studies of the electrocatalytic CO_2 reduction reaction (eCO_2RR) under external magnetic fields [22]. Among the limited existing research, Pan et al. pointed out that a magnetic field could increase the number of singlet radical pairs, thus enhancing the activity of a Sn catalyst for the two-electron reduction of CO_2 to formic acid in the magnetic field [23]. The proposed mechanism by Pan was further updated and expanded by Player et al. with the radical pair spin dynamics simulation method [24]. Additionally, Bhargava et al. found that the overpotential for the eCO_2RR toward CO using a Ni–Fe bimetallic catalyst decreased in a magnetic field on account of the magnetohydrodynamic effect [25]. It should be noted that the mechanistic explanations of the influence of magnetic fields on the eCO_2RR performance enhancement are still primitive and ambiguous, requiring further clarification.

Intuitively, we consider that the origin of the effect of external magnetic fields on current density (reflecting electrocatalytic activity) lies in the magnetic catalysts themselves in response to the external fields

---

* Corresponding author.
E-mail address: lang.xu@cumt.edu.cn (L. Xu).

https://doi.org/10.1016/j.eehl.2024.02.003
Received 29 November 2023; Received in revised form 5 February 2024; Accepted 24 February 2024

(microscopically, the collective effect of the ensemble of electron spins on different metal centers of the magnetic catalysts), whereas the influence of magnetic fields on faradaic efficiency (characterizing electrocatalytic selectivity) needs to be interpreted at the molecular level. To our knowledge, the study of electrocatalytic selectivity in response to external magnetic fields remains unexplored. It is essential to establish the underlying mechanisms at a molecular scale because reactive species involved in numerous electrochemical processes (such as eCO_2RR) are molecules that are associated with electrocatalytic selectivity. On the other hand, magnetic fields provided by regular field sources make molecular structural changes too subtle to be easily detectable, thereby contributing to the heightened complexity of the study.

For these reasons, we now design a magnetic-field-equipped *operando* infrared spectroscopic device and determine magnetic responses of the eCO_2RR driven by the coupling of electric and magnetic fields in this work. Our observations reveal that the application of external magnetic fields at small electric potentials leads to current densities comparable to those achieved at larger potentials in the absence of magnetic fields. Building upon electrochemical impedance spectroscopy (EIS) evidence obtained within a magnetic-field gradient, we can attribute the phenomenon, referred to as “magnetic gain”, to the parallel alignment of individual magnetic moments within a Ni-containing carbonaceous magnet (Ni-CM) upon the application of an external field. Therefore, it is imperative that Ni-CM exhibits responsiveness to the magnetic field and possess a certain level of activity for the eCO_2RR. Furthermore, experimental observations on the magnetic dependence of electrocatalytic selectivity reveal an increase in faradaic efficiency in an applied magnetic field, along with the magnetic-field-induced change in molecular bonding detected by the high-sensitivity *operando* attenuated total reflection surface-enhanced infrared absorption spectroscopy (ATR-SEIRAS). Combined with the density functional theory (DFT) calculations, we can rationalize and explain these trends from a molecular perspective, particularly noting the weakening of the C–O bond strength of the key intermediate *COOH when exposed to a magnetic field.

2. Experimental section

2.1. Synthesis methods

First, 0.45 g of $Zn(NO_3)_2{\cdot}6H_2O$ was dissolved in 3 mL of deionized water (Solution A), and 5.5 g of 2-methylimidazole was dissolved in 20 mL of deionized water (Solution B). Subsequently, Solutions A and B were mixed and stirred for 6 h at room temperature. Then, the resulting mixture was centrifuged twice (each time, 5 min and 5,000 rpm), and dried at 80 °C for 12 h to obtain Sample C. Upon completion, 0.5 g of Sample C and 0.5 g of Ni $(NO_3)_2{\cdot}6H_2O$ were added to 10 mL of an ethanol–water mixture in a volumetric ratio of 1:1 and stirred for 4 h at room temperature. The resulting solid sample was obtained after drying at 80 °C for 12 h. Next, the solid sample was transferred to a tube furnace and heated at 900 °C for 2 h at a ramp rate of 2 °C/min under flowing N_2. After cooling down to room temperature, the black powder was immersed in a dilute HCl solution (1 M) for 2 h at 60 °C and then rinsed with deionized water until the filtrate reached pH neutrality. Finally, the product was dried in an oven at 80 °C for 4 h, denoted Ni-CM. For comparison, a control sample (referred to as CM) was prepared using the same procedure as for Ni-CM, except that $Ni(NO_3)_2{\cdot}6H_2O$ was not included.

2.2. Characterization techniques

Magnetic hysteresis loops were obtained using a Lake Shore 7404 vibrating sample magnetometer (VSM). Surface elemental analysis was conducted using a Thermo Scientific K-Alpha X-ray photoelectron spectrometer (XPS), equipped with Al Kα X-ray (energy = 1,486.6 eV). All binding energies were referenced to the C 1s binding energy of 284.8 eV. X-ray absorption spectroscopy (XAS) measurements at the Ni K-edge were conducted at the 4B9A beamline station of the Beijing Synchrotron Radiation Facility (BSRF), China. Ni foil and nickel phthalocyanine (NiPc) were used as references. *Operando* ATR-SEIRAS data were recorded on a Thermo Scientific Nicolet iS20 Fourier transform infrared (FTIR) spectrometer equipped with a mercury-cadmium-telluride (MCT) detector. The attenuated total reflectance-surface enhanced functionality was achieved on a Pike VEEMAX III variable angle specular reflection accessory.

2.3. Electrochemical measurements in external magnetic fields

A catalyst ink was prepared by dispersing 10 mg of Ni-CM in a mixture of 20 μL of 5 wt% Nafion™ solution and 480 μL of *N,N*-dimethylformamide (DMF), followed by sonication for 1 h. A working electrode was processed by pipetting 80 μL of the catalyst ink onto a hydrophobic carbon paper and air-drying, with a catalyst loading of 0.8 mg/cm^2. An H-type cell separated by a Nafion™ 115 membrane was used as the electrolytic cell for the eCO_2RR. Ag/AgCl and platinum foil were employed as the reference and counter electrodes, respectively. The electrolyte used was an aqueous solution of $KHCO_3$ (0.5 M). Unless otherwise stated, all potentials were given with reference to the reversible hydrogen electrode (RHE) scale using the conversion formula: $E_{\mathrm{RHE}} = E_{\mathrm{Ag/AgCl}} + 0.205\mathrm{V} + 0.059\mathrm{pH}$ (at 25 °C).

External magnetic field sources stem from different numbers of permanent magnets, providing different magnetic strengths of 70, 120, 220 and 320 mT (millitesla) for electrochemical reactions, which were measured by a magnetometer. In the absence or presence of an external magnetic field, chronoamperometric measurements were conducted at selected potentials in 0.5 M $KHCO_3$ saturated with CO_2, while linear sweep voltammograms were recorded at 5 mV/s in a potential range of 0 to −1.1 V in CO_2 or N_2 saturated 0.5 M $KHCO_3$. Additionally, EIS measurements were performed over a frequency range from 10^5 to 10^{-2} Hz at a potential of −0.7 V in the CO_2-saturated 0.5 M $KHCO_3$.

Both quantitative and qualitative analyses of reaction products were conducted using an Agilent 7890B online gas chromatography (GC), equipped with flame ion detectors (FID) and thermal conductivity detectors (TCD). Faradaic efficiency (FE) values were calculated using the following expression:

$$\mathrm{FE} = \frac{n \times V \times v \times F \times P}{I \times R \times T} \times 100\%$$

where F represents the faraday constant (96,485 C/mol), I is the current at a specific electric potential (A), n is the number of transferred electrons (which is 2 for CO_2 and H_2), P is the standard pressure (1.013 × 10^5 Pa), R is the gas constant [8.314 J/(mol·K)], T is the absolute temperature (298.15 K), V is the volume fraction of the product calculated from GC, and v is the gas flow rate (10 mL/min).

2.4. Design of a magnetic-field-equipped operando infrared spectroscopic device

A specialized testing device has been designed in this work to meet the requirement for *operando* infrared spectroscopy measurements in an external magnetic field. Based on the optical path of the FTIR spectrometer, the configurations of electrodes and gas passages are exhibited in Fig. 1a. The electrolytic cell chamber is designed with a concave shape, aiming to allow permanent magnets to be as close as possible to the working electrode (at a distance of 5 mm), ensuring a sufficient magnetic field strength at the working electrode (measured to be 320 mT). It is worth noting that the electrolyte solution is contained inside of the electrolytic cell chamber, while the exterior holds the permanent magnets.

To create a working electrode for the *operando* ATR-SEIRAS measurements, a film of nanoparticulate Au was coated on a Si crystal by the radio frequency (RF) magnetron sputtering method, and then the catalyst

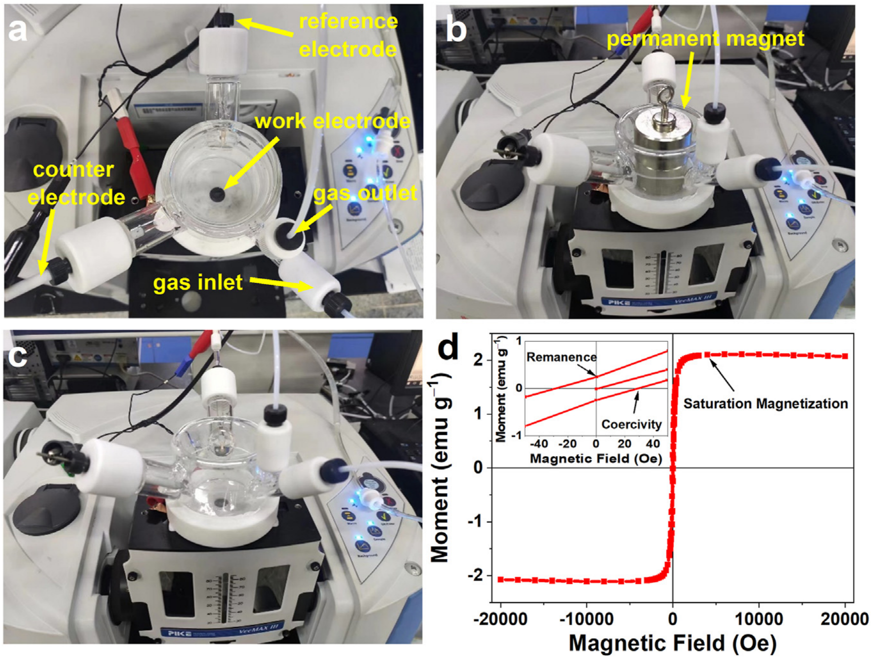

Fig. 1. Photographic images of the magnetic-field-equipped *operando* ATR-SEIRAS device and the magnetic property of Ni-CM. (a) Top view of the electrolytic cell chamber showing the configuration of electrodes and gas passages. (b) *Operando* ATR-SEIRAS measurement in the absence of external magnetic field. (c) *Operando* ATR-SEIRAS measurement in an applied magnetic field provided by a permanent magnet. (d) A magnetic hysteresis loop of Ni-CM. The inset enlarges the region of a near-zero field.

ink was uniformly spray-painted onto the Au film. After air drying, the working electrode was set up at the bottom of the concave electrolytic cell chamber that was installed in the ATR-SEIRAS device (Fig. 1a). The counter and reference electrodes, along with the electrolyte solution, were the same as those used in the H-type cell.

The electric potential applied during the *operando* ATR-SEIRAS analysis was set at −0.7 V. Fig. 1b shows the situation when a permanent magnet is placed in the concavity of the cell, while Fig. 1c depicts the situation when an external magnetic field is absent.

Thus, this well-designed device enables the execution of *operando* ATR-SEIRAS measurements both with and without the application of magnetic fields.

2.5. Computational details

DFT calculations were conducted by the Vienna Ab initio Simulation Package (VASP, version 6.1.0) [26–29]. Projector augmented wave (PAW) pseudopotentials were employed to reflect core and valence electrons. The Perdew–Burke–Ernzerhof (PBE) functional and generalized gradient approximation (GGA) were adopted to describe the exchange correlation between electrons. A 4 × 4 supercell was constructed to represent the Ni(111) surface, with a five-layer slab model utilized. To avoid interactions between adjacent layers, a vacuum layer with a thickness of 25 Å was applied along the *z* axis to the slab. A cutoff energy of 500 eV for the plane-wave basis set was adopted. The Brillouin-zone integration was undertaken with a 4 × 4 × 1 Monkhorst–Pack *k*-point grid. The convergence criteria for force and energy were set to 0.02 eV/Å and 10^{-5} eV, respectively. The free energies of species in the eCO_2RR were calculated by the following equation:

$$G = E_{\mathrm{Total}} + E_{\mathrm{ZPE}} - TS$$

where E_{Total} is the total energy of a species gained from the DFT calculations, E_{ZPE} is zero-point energy, S is entropy, and T is the absolute temperature.

The electroreduction of CO_2 to CO involves multi-step proton-electron transfers, which can be simplified to the following procedures:

$$CO_2 + H^+ + e^- + * \rightarrow *COOH$$

$$*COOH + H^+ + e^- \rightarrow *CO + H_2O$$

$$*CO \rightarrow CO$$

where * is the active site.

Note that because the VASP software cannot directly stimulate the effect of external magnetic fields, electric fields have been substituted for magnetic fields instead as the external fields in this work. The substitution is reasonable because “electric and magnetic forces are part of one physical phenomenon—the electromagnetic interactions of particles. The separation of this interaction into electric and magnetic parts depends very much on the reference frame chosen for the description” [30]. A recent paper published by Gao et al. was also treated in this manner [31]. We thus model a magnetic-field gradient by using different strengths of electric fields. Specifically, we set the electric field strengths to 0, 0.1, 0.3 and 0.4 V/Å to simulate no field, weak field, medium field and strong field, respectively.

3. Results and discussion

3.1. Magnetization curves for the nickel-bearing ferromagnetic electrocatalyst

It is known that Ni(0) exhibits the ferromagnetic behavior at room temperature, which can be characterized by magnetic hysteresis loops [32,33]. As displayed in Fig. 1d, Ni-CM can easily be magnetized and demagnetized. As the applied magnetic field increases, the magnetization (*i.e.*, magnetic moment) of Ni-CM rises to a steady limiting value dramatically (2.1 emu/g), known as saturation magnetization, and retraces its original path when the applied field decreases, with a remanence of 0.24 emu/g and a coercivity of 26.8 Oe (Fig. 1d). The situations under the reverse field (opposite direction) remain the same. The extremely narrow (but nonzero) hysteresis loop, alongside the readily reversible magnetization, demonstrates that Ni-CM is a soft ferromagnet [34]. This immediate response to applied magnetic fields enables Ni-CM to act as the sensitive electrocatalyst in oscillating magnetic fields, which is described in more detail below.

3.2. *Magnetic dependence of current density*

The impacts of applied magnetic fields on the electrochemical reaction rates (expressed in terms of apparent current density that is a summation of catalytic, charging, and other possible components of current flows) are first examined using a chronoamperometric approach. As shown in Fig. 2a, the apparent current densities of Ni-CM in the eCO_2RR process are highly sensitive to the periodic variations in the oscillating magnetic fields. The apparent current densities increase abruptly to the flat plateaus when the magnetic fields are applied, and it is found that the higher the magnetic field strengths, the greater the current density increments. Once the magnetic fields are removed, the apparent current densities immediately return to their original values, which can be attributed to the soft ferromagnetism of Ni(0) in Ni-CM. The chronoamperometric responses to the on-off switches of applied magnetic fields demonstrate that it is the external magnetic fields that change the apparent current densities for the eCO_2RR. By comparing the apparent current densities of Ni-CM at different magnetic field strengths and electric potentials (Fig. 2a), it follows that the external magnetic fields enable the ferromagnetic electrocatalyst to obtain higher current densities at less negative potentials. This implies that less electric energy is required to reach the same electrochemical reaction rates in the magnetic field, a phenomenon called magnetic gain.

To delve deeply into the chronoamperometric responses to the oscillating magnetic fields, magnetocurrent densities, which are defined as the subtraction of current densities in the absence of applied magnetic fields (j) from those generated in the magnetic fields (j_m), *i.e.*, j_m–j, can be obtained from Fig. 2a. At each electric potential, the magnetocurrent densities of Ni-CM increase as the magnetic field strength is raised (Fig. 2b and Table S1), displaying a positive correlation between the magnetocurrent densities and the magnetic field strengths. In addition, a second parameter, varying percentage of magnetocurrent densities, expressed by writing $\frac{j_m-j}{j} \times 100\%$, is found to increase first and then decrease with increasing applied electric potentials (Fig. 2c). Such a trend can be rationalized by the presence of the Coulombic repulsion. Specifically, driving the ferromagnetic electrocatalyst to more negative potentials leads to a noticeable increase in current densities (*i.e.*, moving electrons), hence intensifying the accumulation of electrons and resulting in the strengthening of the Coulombic repulsion between electrons. In this sense, the incremental changes of magnetocurrent densities with increasing applied electric potentials are counteracted by a progressive increase in the electrostatic repulsion, causing the varying percentages of magnetocurrent densities to dwindle as the electric potentials move toward more negative values (Fig. 2c).

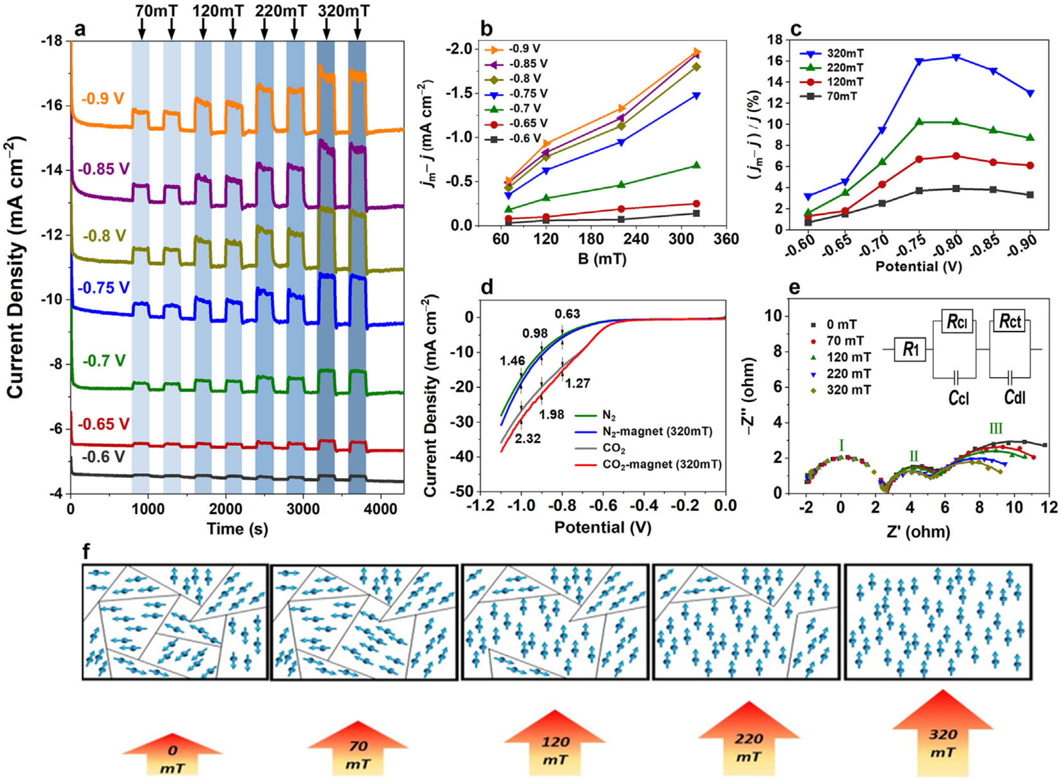

Fig. 2. Current densities for the eCO_2RR in response to applied magnetic fields. (a) Responses of apparent current densities of Ni-CM at different electric potentials to on-off switches of applied magnetic fields with varied strengths. (b) Dependence of magnetocurrent densities of Ni-CM at different electric potentials on magnetic field strengths. (c) Dependence of varying percentages of magnetocurrent densities of Ni-CM with different magnetic field strengths on electric potentials. (d) Linear sweep voltammogram of Ni-CM with and without an external magnetic field of 320 mT in the N_2- and CO_2-saturated electrolytes. (e) Nyquist plots of Ni-CM in the external magnetic fields with different strengths (320, 220, 120, 70 and 0 mT) at an electric potential of −0.7 V in the CO_2-saturated electrolyte and their corresponding best–fit curves for the equivalent circuit, as shown in the inset. (f) A schematic illustration of the extent of parallel alignment of individual magnetic moments with different magnetic field strengths.

To establish whether the increases in apparent current densities at applied magnetic fields have contributions from the eCO_2RR, we carried out voltammetric experiments with and without CO_2. Fig. 2d shows the linear sweep voltammograms for Ni-CM in the N_2- and CO_2-saturated solutions using or dispensing with a magnetic field of 320 mT. The rise of current densities induced by the external magnetic field (*i.e.*, magnetocurrent densities) in both N_2 and CO_2 can easily be observed when the electric potentials decrease to approximately -0.6 V or lower. The corresponding values of magnetocurrent densities at different electric potentials are indicated on either side of the voltammograms in Fig. 2d. The magnetocurrent densities in N_2 are expected to emerge from the growth of charging currents in the applied magnetic fields, which can be validated by an impedance method that is described below. At the same electric potentials, the magnetocurrent densities in CO_2 are consistently higher than in N_2, which is a consequence of the fact that the eCO_2RR does take place in the former case. In other words, the eCO_2RR indeed responds to external magnetic fields.

To differentiate between the magnetocurrent contribution of eCO_2RR and its competitor–hydrogen evolution reaction (HER), we compared the partial current densities for CO and H_2 production with and without the magnetic field. As shown in Fig. S1, the partial current density for CO production markedly increases by 1.44 mA/cm^2 upon the application of a 320 mT magnetic field; by comparison, the partial current density for the H_2 production increases by only 0.36 mA/cm^2 under the same conditions. Comparisons of the partial current densities of CO and H_2 production with and without the magnetic field reveal that the magnetic field effectively enhances both eCO_2RR and HER. However, it exhibits a notably stronger effect in increasing the CO partial current density, attributed to the effectiveness of Ni-CM as a magnetic catalyst for eCO_2RR, which effectively inhibits HER. Interestingly, the Ni-free material CM undergoes the magnetically induced fluctuations in current density upon the application of the external magnetic field (Fig. S2), indicating that the capability of magnetic fields for increasing current densities can seem universal in the sense that magnetocurrent densities are composed of electrocatalytic, charging or other types of contributions.

So why can external magnetic fields influence current densities? We hypothesize that a gradual variation of charge-transfer resistance is modulated by changes in magnetic field strengths. The electrocatalytic reduction of CO_2 is accompanied by charge transfer. Whether and how an external magnetic field impacts charge transfer was investigated using the EIS approach. Generally, the EIS experiments are undertaken at an open circuit, but in this study, they were performed at a working potential of the catalyst (-0.7 V) instead. This is because no current flows at an open circuit (*i.e.*, no moving charges), and the applied magnetic field cannot affect static charges. Fig. 2e shows the Nyquist plots of Ni-CM at different magnetic field strengths (0 → 320 mT) and their corresponding best–fit curves for the equivalent circuit (as depicted in the inset to Fig. 2e). Each Nyquist plot takes on three semicircles, which are sequentially denoted I, II and III from high to low frequencies. Notably, Semicircle I at the higher frequencies enters the negative part of the real axis, which is very rare in conventional operations at open circuits. This observation can be explained on the grounds that the eCO_2RR is occurring at this applied electric potential. Kubannek et al. reported that a dead time (Δt) between the formation and detection of a reaction product led to an increase in phase shift ($\Delta\varphi$) with frequency (f), which could be described by the expression $\Delta\varphi = \Delta t \cdot f$. They pointed out that the negative real component of impedance would appear at increasing f when $\Delta\varphi > \pi/2$ [35]. Thus, the rising f results in increasing $\Delta\varphi$ in situations where Δt is not zero (because the eCO_2RR happens), and the Nyquist plot finally reaches the negative real part after $\Delta\varphi$ exceeds the critical point ($\pi/2$). Moreover, according to the equivalent circuit, Semicircle II is attributed to a parallel combination of catalyst-layer resistance (R_{cl}) and catalyst-layer capacitance (C_{cl}), whereas Semicircle III stems from a parallel circuit of charge-transfer resistance (R_{ct}) and double-layer capacitance (C_{dl}) [36]. It is noteworthy that Semicircle III shows a significant difference in diameter at varying magnetic field strengths compared to the other two semicircles, signifying that charge transfer and electrical double layer are strongly influenced by external magnetic fields. As shown in Table S2, C_{dl} increases in the presence of applied magnetic fields, which is consistent with the discussion of the charging component in magnetocurrent densities described earlier, while R_{ct} decreases as the magnetic field strength increases, which can be rationalized in terms of the existence of magnetic domains. In the magnetic domain of a ferromagnet, electron spins on individual magnetic centers are coupled into a parallel alignment. As illustrated in Fig. 2f, increasing field strength leads to further alignment of different domains and therefore longer-range ordering of magnetic moments, capable of reducing the scattering of conduction electrons and hence R_{ct} [37]. As a result, the decreasing R_{ct} leads to the increasing current density at fixed potentials as the magnetic field strength rises.

Furthermore, it is found that R_{ct} continues to decrease rapidly but then reaches a plateau as the magnetic field strength increases from 320 mT through 500 mT to 1,000 mT, as shown in Fig. S3. This trend can be explained by considering the correlation between the alignment of magnetic moments and the magnetic field strength. As exhibited in the magnetic hysteresis loop of Ni-CM (Fig. 1d), when the magnetic field strength reaches 500 mT (equivalent to 5,000 Oe), saturation magnetization occurs, indicating that the alignment of magnetic moments reaches a maximum at 500 mT and that the long-range ordering of magnetic moments is also at the maximum. Because the increase in long-range ordering of magnetic moments can give rise to the decrease in the scattering of conduction electrons, R_{ct} rapidly reaches the minimum as the magnetic field strength increases from 0 mT to 500 mT and then remains almost unchanged beyond 500 mT. In this sense, the EIS data are fully consistent with the magnetic hysteresis property, demonstrating that our approach to investigate the influence of magnetic field on electrocatalytic activity from the perspective of the alignment of magnetic moments is scientifically sound.

Additionally, the eCO_2RR shows good stability for an extended period of time upon application of an external magnetic field (Fig. S4), exhibiting the long-term stability of the current response for the eCO_2RR embedded in the magnetic field.

3.3. Chemical states of Ni-CM

As described above, given that the influence of magnetic fields on the eCO_2RR activity (as measured by current density) is to a large extent exerted through the magnetic response of Ni-CM, it is pertinent to delve into the chemical states of this soft ferromagnetic electrocatalyst. The XPS survey spectrum of Ni-CM provides meaningful information on its surface elemental composition, containing various quantities of elements, including C, N, O and Ni (Fig. S5). As presented in Fig. 3a, the high-resolution XPS spectra of Ni $2p_{3/2}$ and $2p_{1/2}$ from Ni-CM can each be deconvoluted into two peaks, which are assigned to Ni(0) and Ni(II) [38], indicating the presence of these two oxidation states on the surface nickel. Subsequently, we conducted the XAS analysis to investigate the chemical state of the overall nickel. Fig. 3b showcases the Ni K-edge X-ray absorption near-edge structure (XANES) spectra of Ni-CM along with two reference materials Ni foil and NiPc, representing Ni(0) and Ni(II), respectively. Since a higher oxidation state causes an absorption edge to shift toward a higher energy, it follows that edge position, which is defined as energy at the half-height of a recorded edge curve, serves as a descriptor for estimating the oxidation state [39,40]. As exhibited in the inset to Fig. 3b, the edge position of Ni-CM lies between those of Ni foil and NiPc (more precisely, much closer to that of Ni foil), signifying that the oxidation state of Ni-CM falls between Ni(0) and Ni(II), with the majority of Ni being in the Ni(0) state. Furthermore, the first derivatives of XANES spectra provide another useful guide as to the relative sizes of the oxidation states [40,41]. Fig. 3c shows the differentiation of absorption with respect to energy for the Ni K-edge XANES spectra of Ni-CM

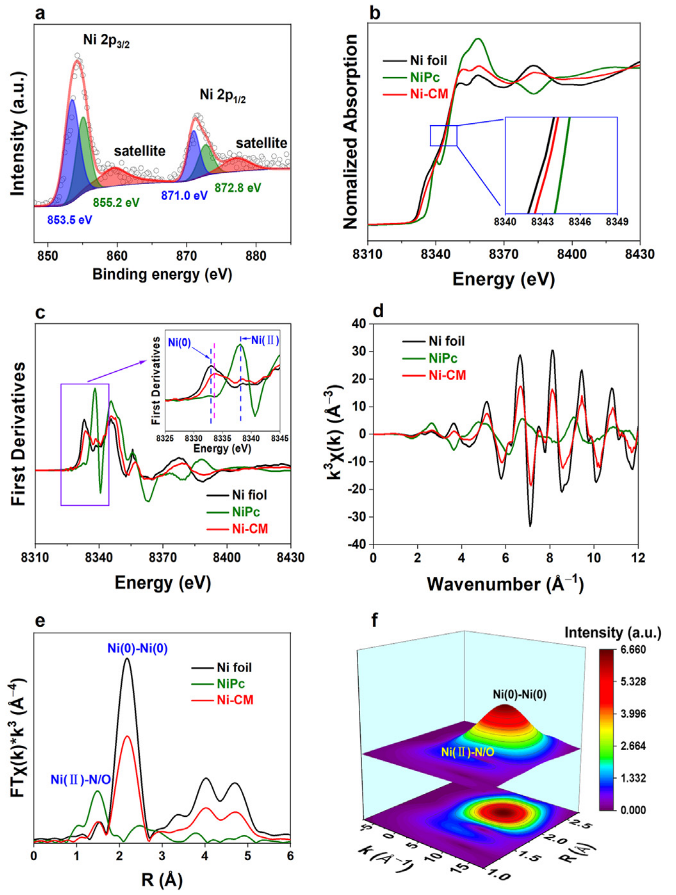

Fig. 3. Chemical states of the ferromagnetic electrocatalyst. (a) High-resolution XPS spectra of Ni $2p_{3/2}$ and $2p_{1/2}$ of Ni-CM. (b) Ni K-edge XANES spectra of Ni-CM, Ni foil and NiPc. The inset displays a magnified view of the edge positions of the three samples. (c) First derivatives of the Ni K-edge XANES spectra from (b). The enlarged inset shows the low-energy peak positions marked by dashed vertical lines. (d) K-space EXAFS spectra of Ni-CM, Ni foil and NiPc. (e) Fourier-transformed R-space EXAFS spectra of Ni-CM, Ni foil and NiPc. (f) Wavelet transformation of the Ni K-edge EXAFS spectra of Ni-CM, portraying the scattering contributions from the Ni(0)–Ni(0) and Ni(II)–N/O bonds in the two-dimensional (lower) and three-dimensional (upper) representations.

alongside the two reference materials. It is obvious from the dashed vertical lines (marking the peak positions in the low-energy region) that the main oxidation state of Ni-CM is Ni(0), as presented in the inset of Fig. 3c. In addition to XANES, another region of XAS spectra frequently used for probing bonding information is extended X-ray absorption fine structure (EXAFS). The k-space EXAFS spectra of Ni-CM, Ni foil and NiPc present excellent signal-to-noise ratios (Fig. 3d), indicating high-quality data [40]. The Fourier transformation of k-space data gives rise to the corresponding real-space (R-space) EXAFS spectra. Fig. 3e displays the Ni K-edge Fourier-transformed R-space EXAFS spectra of the three samples. It is observed that the main peaks of the reference materials Ni foil (at 2.18 Å) and NiPc (at 1.47 Å) can be attributed to the scattering paths of the Ni(0)–Ni(0) and Ni(II)–N/O bonds, respectively [42,43]. The two neighboring elements N and O involved in the symbol Ni(II)–N/O can be rationalized on the basis that there is almost no clear distinction between metal−N and metal−O bonds from the EXAFS spectra [39,40]. For Ni-CM, its main peak at 2.18 Å is the same as for Ni foil, showing that Ni-CM is believed to contain a very high extent of the Ni(0)–Ni(0) bond, which is consistent with the XANES data as described earlier. It is worth noting that the minor peaks from both Ni-CM and Ni foil appear at 1.47 Å, where the main peak of NiPc is observed, indicating that Ni-CM has small quantities of the Ni(II)–N/O bond (the reason why the EXAFS spectrum of Ni foil also shows this minor peak is due to the fact that a passivation layer of nickel oxide is naturally formed on its surface). To provide a vivid portrayal of the relative proportions of the Ni(0)–Ni(0) and Ni(II)–N/O bonds in Ni-CM, we carried out the wavelet transformation of its EXAFS spectrum, which often yields a two-dimensional visualization of the spectrum under investigation by a combination of k-space and R-space [39]. The lower diagram in Fig. 3f displays the Ni K-edge wavelet-transformed EXAFS spectrum of Ni-CM, with the contour level representing the intensity. In the upper diagram, a three-dimensional representation allows for a quick assessment of the relative intensities of different bonding types. It is evident that the intensity of the Ni(0)–Ni(0) bond is significantly higher than that of Ni(II)–N/O, indicating that nickel is largely present as nanoparticulate Ni(0) in Ni-CM. This finding is consistent with the XRD result, which suggests that nickel in Ni-CM mostly exists as the form of an elemental metal (Fig. S6).

Consequently, it is those chemical states that engender the magnetic dependence of current density: because the overwhelming majority of nickel in Ni-CM is Ni(0), the soft ferromagnetism arising from Ni(0) enables this magnetic catalyst to respond rapidly to the oscillating magnetic fields; furthermore, the degree of ordering of magnetic moments in Ni-CM increases as the magnetic field strength is raised, leading to the reduction of conduction-electron scattering and charge-transfer resistance.

3.4. *Magnetic dependence of faradaic efficiency*

How does an applied magnetic field affect the faradaic efficiency of eCO_2RR? To answer this question, we measured the faradaic efficiencies for the eCO_2RR toward CO (abbreviated FEco) catalyzed by Ni-CM with and without the presence of a magnetic field. To ensure the reliability of data, the FEco values were collected and calculated using a method involving multicycle on-off switches of the magnetic field (noting that one cycle refers to a half–hour reaction without any external magnetic field and another half–hour reaction in the presence of a magnetic field of 320 mT). Fig. 4a presents the fluctuations in FEco at different electric potentials after the application (marked with stars) and removal (marked with dots) of the magnetic field for five switching cycles, with the corresponding values being summarized in Table S3. It can be observed that the variation in FEco at each electric potential follows the same trend, namely an increase in FEco after the application of the magnetic field to Ni-CM, followed by a decrease after the removal of the applied field. The cyclic behavior of the magnetic responses of FEco is consistent across data sets: the increments and decrements are nearly identical between each cycle, showing the repeatability, reversibility and stability of FEco upon application of the magnetic field and also providing strong evidence that the magnetic field can indeed enhance FEco.

To understand how an external magnetic field raises FEco and determine the mechanism at the molecular level, we monitored the progress of eCO_2RR occurring at the surface of Ni-CM under magnetic and nonmagnetic conditions, by employing the magnetic-field-equipped *operando* ATR-SEIRAS technique (Fig. 4b). The *operando* ATR-SEIRAS spectra reveal the C–O stretching vibration of the key intermediate *COOH in terms of eCO_2RR (Fig. 4c) [44], regardless of the presence of an applied magnetic field. Upon magnification of the C–O region in selected spectra, it can be observed from Fig. 4d that after the application of the magnetic field of 320 mT, the stretching vibration band of C–O, originally at 1,235 cm^{-1}, shifts to a lower wavenumber (1,223 cm^{-1}), *i.e.*, red shift. This shift suggests that the external magnetic field weakens the C–O bond strength and elongates the C–O bond length. This subtle change facilitates the dissociation of the C–O bond, thereby promoting the generation of CO and increasing FEco.

To further investigate the underlying mechanism of the impact of applied magnetic field on faradaic efficiency, we simulated the thermodynamic processes of eCO_2RR with different external field strengths by the DFT method. As mentioned above, the reaction intermediate *COOH has been identified by the *operando* ATR-SEIRAS spectra. The formation of *COOH is the potential-determining step for the eCO_2RR toward CO,

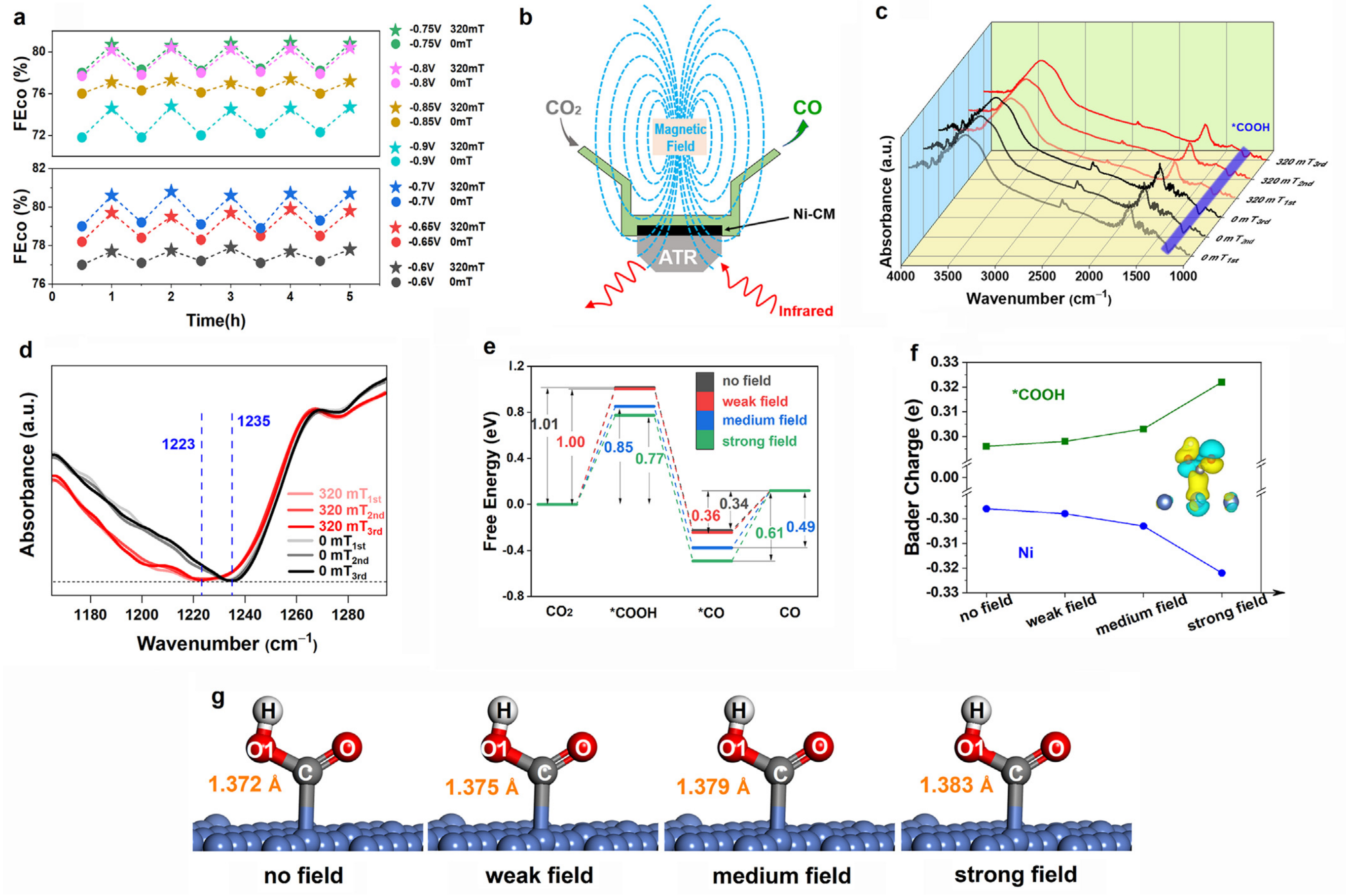

Fig. 4. Response of FEco to external magnetic fields. (a) Variations of FEco of Ni-CM with 5-cycle on-off switches of the magnetic field (320 mT) at different electric potentials. The FEco values obtained in the magnetic field are indicated by ★, whereas those without any magnetic field are marked by •. (b) A schematic representation of the magnetic-field-equipped *operando* ATR-SEIRAS device. (c) *Operando* ATR-SEIRAS spectra of Ni-CM that is being acted as a working catalyst for the eCO_2RR in the presence and absence of the magnetic field (320 mT). Spectra were scanned three times for each situation. The C–O stretching vibration bands of the key intermediate *COOH are highlighted. (d) A magnified view of the *operando* ATR-SEIRAS spectra from c in the range between 1160 and 1300 cm^{-1}. (e) Gibbs energy profiles of eCO_2RR toward CO on Ni with different external field strengths. The energy barriers of the elementary steps are indicated. (f) Variations in Bader charges of Ni and *COOH in response to external fields with different strengths. The Bader charge distribution between Ni and *COOH in the strong field is shown. (g) Changes of chemical structures of *COOH on Ni with different external field strengths. The C–O1 bond lengths are marked.

because it has the highest free energy barrier, as exhibited in Fig. 4e. Lowering the energy barrier of the potential-determining step makes the reaction more energetically favorable [45]. Additionally, it is observed from Fig. 4e that compared to the absence of an external field, the application of the field can effectively reduce the free energy barriers for *COOH, with a gradually increasing reduction in the height of the energy barrier as the external field strength is raised, thereby facilitating the occurrence of the CO_2-to-CO reaction.

From the experiment, the *operando* ATR-SEIRAS spectra have demonstrated that *COOH does indeed undergo a subtle change in structure when exposed to an external magnetic field, suggesting a close relationship between the variation in the energy barrier for the potential-determining step and the external field strength with the alteration in the chemical structure of *COOH. To prove this, we probed the correlation of charge distribution and molecular structure with external field strength. Fig. 4f shows the dependence of the Bader charge distributions between *COOH and Ni on the external field strengths. As the field strength increases, the partial charge is shifted from Ni to *COOH, resulting in a decrease in the charge density around Ni and an attendant increase in the charge density on the *COOH species. In other words, the external field modulates the charge distribution on the key intermediate. The variation in the charge distribution, in turn, leads to a change in the molecular structure. As presented in Fig. 4g, the length of the C–O bond (labeled as C–O1) in *COOH increases under the influence of the external field, which is consistent with the phenomenon observed in the *operando* ATR-SEIRAS measurements. Furthermore, it can be shown that the greater the external field strength, the longer the C–O bond length. In short, the *elongation* of the C–O bond induced by the external field implies a weakening of the chemical bonding, giving rise to a decrease in the energy required for the bond breaking.

4. Conclusions

We have systematically and thoroughly explored the kinetics, energetics and mechanisms of the eCO_2RR in response to the magnetic-field gradient. The significance of this work can now be summarized as follows:

1) The applied magnetic fields have been shown to be able to enlarge both catalytic and charging currents (the stronger the magnetic field strength, the greater the current density increment). Furthermore, it has been demonstrated that strengthening magnetic fields gives rise to the longer-range ordering of magnetic moments, thereby decreasing the scattering of conduction electrons and charge-transfer resistances.

2) Through the action of the magnetic-field gradient, the intriguing phenomenon known as magnetic gain has been identified: the same level of current density obtained at a large electric potential can be achieved

by applying an external magnetic field at a small potential, resulting in a significant reduction in energy consumption. In addition, the property of soft ferromagnetism allows for the instantaneous current responses to the on-off (oscillating) switches of external magnetic fields.

3) The well-designed magnetic-field-equipped *operando* ATR-SEIRAS device has successfully captured the subtle changes in molecular structures upon the application of magnetic fields. This addresses the challenge of the acquisition of barely perceptible molecular structural changes in response to applied magnetic fields, enabling the elucidation of the underlying mechanism by which the magnetic fields affect the catalytic selectivity at the molecular level.

4) The external magnetic fields have proven capable of modulating charge distributions between active sites and reaction species, therefore leading to a minor perturbation of the molecular structure of the key intermediate *COOH. This slight change in turn influences the energy barrier of the potential-determining step for the eCO_2RR, rendering the reaction energetically favorable and thus promoting an increase in the FEco.

As a consequence, the methods and results presented in this work give us fresh perspectives on the eCO_2RR research and deep mechanistic insights into the underlying mechanism of how external magnetic fields influence electrocatalytic reactions. This yields a blueprint for investigating and elucidating some of the most interesting and unusual examples of molecular structures and bonding in magnetic fields.

CRediT authorship contribution statement

S.W.: data curation, formal analysis, investigation, software, validation, visualization, writing–original draft, writing–review and editing. W.L.: formal analysis, investigation, validation, visualization. P.B.: formal analysis, investigation, software. C.Y.: validation, visualization. X.K.: formal analysis. L.X.: conceptualization, funding acquisition, methodology, project administration, resources, supervision, writing–original draft, writing–review and editing.

Declaration of competing interests

The authors declare no conflict of interests.

Acknowledgments

This work was financially supported by the Fundamental Research Funds for the Central Universities (2023ZDPY04).

Appendix A. Supplementary data

Supplementary data to this article can be found online at https://doi.org/10.1016/j.eehl.2024.02.003.

References

[1] E.M. Purcell, D.J. Morin, Electricity and Magnetism, third ed., Cambridge University Press, 2013, pp. 431–440.

[2] S. Luo, K. Elouarzaki, Z.J. Xu, Electrochemistry in magnetic fields, Angew. Chem. Int. Ed. 61 (2022) e202203564.

[3] H.-B. Zheng, Y.-L. Wang, P. Zhang, F. Ma, P.-Z. Gao, W.-M. Guo, et al., Multiple effects driven by AC magnetic field for enhanced electrocatalytic oxygen evolution in alkaline electrolyte, Chem. Eng. J. 426 (2021) 130785.

[4] J. Yan, Y. Wang, Y. Zhang, S. Xia, J. Yu, B. Ding, Direct magnetic reinforcement of electrocatalytic ORR/OER with electromagnetic induction of magnetic catalysts, Adv. Mater. 33 (2021) 2007525.

[5] W. Kiciński, J.P. Sęk, E. Matysiak-Brynda, K. Miecznikowski, M. Donten, B. Budner, et al., Enhancement of PGM-free oxygen reduction electrocatalyst performance for conventional and enzymatic fuel cells: the influence of an external magnetic field, Appl. Catal. B Environ. 258 (2019) 117955.

[6] Y. Zhang, P. Guo, S. Li, J. Sun, W. Wang, B. Song, et al., Magnetic field assisted electrocatalytic oxygen evolution reaction of nickel-based materials, J. Mater. Chem. A 10 (2022) 1760–1767.

[7] Y. Li, L. Zhang, J. Peng, W. Zhang, K. Peng, Magnetic field enhancing electrocatalysis of Co_3O_4/NF for oxygen evolution reaction, J. Power Sources 433 (2019) 226704.

[8] Z. Fang, W. Zhao, T. Shen, D. Qiu, Y. Lv, X. Hou, et al., Spin-modulated oxygen electrocatalysis, Precis. Chem. 1 (2023) 395–417.

[9] F.A. Garcés-Pineda, M. Blasco-Ahicart, D. Nieto-Castro, N. López, J.R. Galán-Mascarós, Direct magnetic enhancement of electrocatalytic water oxidation in alkaline media, Nat. Energy 4 (2019) 519–525.

[10] X. Ren, T. Wu, Y. Sun, Y. Li, G. Xian, X. Liu, et al., Spin-polarized oxygen evolution reaction under magnetic field, Nat. Commun. 12 (2021) 2608.

[11] X. Ren, T. Wu, Z. Gong, L. Pan, J. Meng, H. Yang, et al., The origin of magnetization-caused increment in water oxidation, Nat. Commun. 14 (2023) 2482.

[12] S. Wei, W. Liu, C. Yang, P. Bai, X. Kong, W. Sun, et al., Electronic and geometric modulations of catalysts for electrochemical CO_2 reduction reaction, Mater. Chem. Front. 7 (2023) 4723–4743.

[13] J. Fu, P. Li, Y. Lin, H. Du, H. Liu, W. Zhu, et al., Fight for carbon neutrality with state-of-the-art negative carbon emission technologies, Eco-Environ. Health 1 (2022) 259–279.

[14] J. Liu, Y. Cai, R. Song, S. Ding, Z. Lyu, Y.-C. Chang, et al., Recent progress on single-atom catalysts for CO_2 electroreduction, Mater. Today 48 (2021) 95–114.

[15] S. Banerjee, C.S. Gerke, V.S. Thoi, Guiding CO_2RR selectivity by compositional tuning in the electrochemical double layer, Acc. Chem. Res. 55 (2022) 504–515.

[16] J. Liu, X. Guo, Z. Lyu, R.-B. Song, P. Zhou, S. Ding, et al., A novel tandem reactor design based on nano-Cu electrocatalysts and microbial biocatalysts for converting CO_2 into ethylene and acetate, Green Chem. 25 (2023) 5712–5720.

[17] J. Zhang, X. Tang, Y. Hong, G. Chen, Y. Chen, L. Zhang, et al., Carbon-based single-atom catalysts in advanced oxidation reactions for water remediation: from materials to reaction pathways, Eco-Environ. Health. 2 (2023) 47–60.

[18] X. Wang, P. Li, Y. Cao, W. Hong, Z. Geng, Z. An, et al., Techno-economic analysis and industrial application prospects of single-atom materials in CO_2 catalysis, Chem. J. Chin. Univ. 43 (2022) 20220347.

[19] L. Xie, Y. Jiang, W. Zhu, S. Ding, Y. Zhou, J.-J. Zhu, Cu-based catalyst designs in CO_2 electroreduction: precise modulation of reaction intermediates for high-value chemical generation, Chem. Sci. 14 (2023) 13629–13660.

[20] A. Zakharchenko, N. Guz, A.M. Laradji, E. Katz, S. Minko, Magnetic field remotely controlled selective biocatalysis, Nat. Catal. 1 (2018) 73–81.

[21] K. Wang, Q. Yang, H. Zhang, M. Zhang, H. Jiang, C. Zheng, J. Li, Recent advances in catalyst design and activity enhancement induced by a magnetic field for electrocatalysis, J. Mater. Chem. A 11 (2023) 7802–7832.

[22] J. Yao, W. Huang, W. Fang, M. Kuang, N. Jia, H. Ren, et al., Promoting electrocatalytic hydrogen evolution reaction and oxygen evolution reaction by fields: effects of electric field, magnetic field, strain, and light, Small Methods 4 (2020) 2000494.

[23] H. Pan, X. Jiang, X. Wang, Q. Wang, M. Wang, Y. Shen, Effective magnetic field regulation of the radical pair spin states in electrocatalytic CO_2 reduction, J. Phys. Chem. Lett. 11 (2020) 48–53.

[24] T.C. Player, P.J. Hore, Source of magnetic field effects on the electrocatalytic reduction of CO_2, J. Chem. Phys. 153 (2020) 084303.

[25] S.S. Bhargava, D. Azmoodeh, X. Chen, E.R. Cofell, A.M. Esposito, S. Verma, et al., Decreasing the energy consumption of the CO_2 electrolysis process using a magnetic field, ACS Energy Lett. 6 (2021) 2427–2433.

[26] G. Kresse, J. Hafner, Ab initio molecular dynamics for liquid metals, Phys. Rev. B 47 (1993) 558–561.

[27] G. Kresse, J. Hafner, Ab initio molecular-dynamics simulation of the liquid-metal-amorphous-semiconductor transition in germanium, Phys. Rev. B 49 (1994) 14251–14269.

[28] G. Kresse, J. Hafner, Efficiency of ab-initio total energy calculations for metals and semiconductors using a plane-wave basis set, Comput. Mater. Sci. 6 (1996) 15–50.

[29] G. Kresse, J. Hafner, Efficient iterative schemes for ab initio total-energy calculations using a plane-wave basis set, Phys. Rev. B 54 (1996) 11169–11186.

[30] R.P. Feynman, R.B. Leighton, M. Sands, The Feynman Lectures on Physics, Volume II, Basic Books, New Millennium Edition, 2010 (Chapter 13)-6.

[31] W. Gao, J. Lu, S. Zhang, X. Zhang, Z. Wang, W. Qin, et al., Suppressing photoinduced charge recombination via the Lorentz force in a photocatalytic system, Adv. Sci. 6 (2019) 1901244.

[32] F. Al Ma'Mari, T. Moorsom, G. Teobaldi, W. Deacon, T. Prokscha, H. Luetkens, et al., Beating the Stoner criterion using molecular interfaces, Nature 524 (2015) 69–73.

[33] Z. Ma, M. Yue, H. Liu, Z. Yin, K. Wei, H. Guan, et al., Stabilizing hard magnetic $SmCo_5$ nanoparticles by N-doped graphitic carbon layer, J. Am. Chem. Soc. 142 (2020) 8440–8446.

[34] J.M.D. Coey, Magnetism and Magnetic Materials, Cambridge University Press, 2010, pp. 439–440.

[35] F. Kubannek, U. Krewer, Studying the interaction of mass transport and electrochemical reaction kinetics by species frequency response analysis, J. Electrochem. Soc. 167 (2020) 144510.

[36] Y. Hao, X. Zhang, Q. Yang, K. Chen, J. Guo, D. Zhou, et al., Highly porous defective carbons derived from seaweed biomass as efficient electrocatalysts for oxygen reduction in both alkaline and acidic media, Carbon 137 (2018) 93–103.

[37] N.A. Spaldin, Magnetic Materials: Fundamentals and Applications, second ed., Cambridge University Press, 2011, pp. 156–168.

[38] L. Cheng, H. Yin, C. Cai, J. Fan, Q. Xiang, Single Ni atoms anchored on porous few-layer g-C_3N_4 for photocatalytic CO_2 reduction: the role of edge confinement, Small 16 (2020) 2002411.

[39] J. Timoshenko, B.R. Cuenya, *In situ/operando* electrocatalyst characterization by X-ray absorption spectroscopy, Chem. Rev. 121 (2021) 882–961.

[40] M. Wang, Z. Feng, Pitfalls in X-ray absorption spectroscopy analysis and interpretation: a practical guide for general users, Curr. Opin. Electrochem. 30 (2021) 100803.

[41] Z. Weng, Y. Wu, M. Wang, J. Jiang, K. Yang, S. Huo, et al., Active sites of copper-complex catalytic materials for electrochemical carbon dioxide reduction, Nat. Commun. 9 (2018) 415.

[42] Y. Hou, Y.-L. Liang, P.-C. Shi, Y.-B. Huang, R. Cao, Atomically dispersed Ni species on N-doped carbon nanotubes for electroreduction of CO_2 with nearly 100% CO selectivity, Appl. Catal. B Environ. 271 (2020) 118929.

[43] C.F. Wen, F. Mao, Y. Liu, X.Y. Zhang, H.Q. Fu, L.R. Zheng, et al., Nitrogen-stabilized low-valent Ni motifs for efficient CO_2 electrocatalysis, ACS Catal. 10 (2020) 1086–1093.

[44] X. Zhang, L. Chen, L. Yuan, R. Liu, D. Li, X. Liu, et al., Conformation-dependent coordination of carboxylic acids with Fe_3O_4 nanoparticles studied by ATR-FTIR spectral deconvolution, Langmuir 35 (2019) 5770–5778.

[45] M.T.M. Koper, Analysis of electrocatalytic reaction schemes: distinction between rate-determining and potential-determining steps, J. Solid State Electrochem. 17 (2013) 339–344.